High-frequency acoustic land full-waveform inversion: a case study from the Sultanate of Oman

A. Sedova[1]*, G. Royle[1], T. Allemand[1], G. Lambaré[1] and O. Hermant[1] demonstrate the ability of acoustic land FWI to recover a high-resolution velocity model on a case study, using reflected waves in addition to diving waves and inverting up to 13 Hz.

Introduction

Applications of full-waveform inversion (FWI) to land seismic data exhibit specific challenges, largely associated with elastic effects and near-surface heterogeneities. This explains why only a few land FWI case studies have been published to date (Mothi et al., 2012; Mei et al., 2014). In recent years, the acquisition design of land surveys has improved dramatically and now offers ideal conditions for FWI: dense sampling, long offsets and full azimuths (FAZ), and very low frequencies down to 1.5 Hz (Mahrooqi et al., 2012). The first published application of 3D land FWI to this new, ultra-low frequency, data set was encouraging (Stopin et al., 2014). The authors demonstrated the capability to recover the long spatial wavelength components of the velocity model, robustly and efficiently, using diving wave FWI and basic data pre-processing. It was proposed that the resulting velocity model be used as a starting model for reflection-based tomography. Limitations in obtaining a high-resolution velocity model (> 6 Hz) from FWI were identified, and attributed to the acoustic assumption and a weak signal-to-noise ratio.

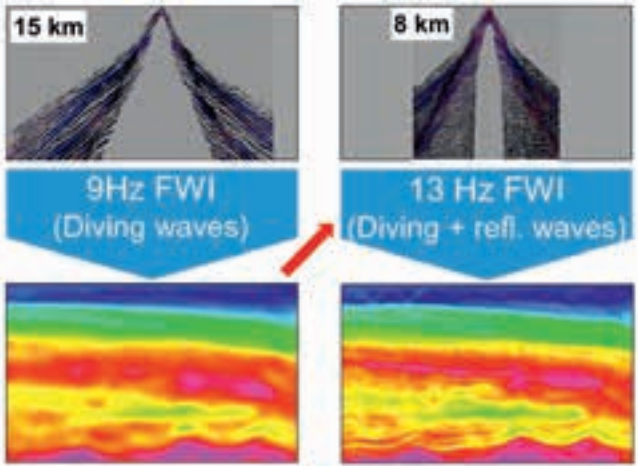

Figure 1 Our acoustic land FWI workflow. We propose a two-stage FWI approach which initially focuses on refractions and diving waves and subsequently incorporates reflections with a maximum frequency of 13 Hz. The long spatial wavelength components of the velocity model are recovered before the shorter spatial wavelengths to reduce the likelihood of cycle-skipping and allow the algorithm to obtain high-resolution details typically observed only in marine case studies.

In this paper, we demonstrate the ability of acoustic land FWI to recover a high-resolution velocity model on a similar case study, using reflected waves in addition to diving waves and inverting up to 13 Hz. A critical step is the pre-processing of the diving and reflected waves, which aims to enhance data coherency at low frequencies and remove surface-related noise. Rather than applying multi-parameter FWI as used in Stopin et al. (2014), we estimate anisotropy using joint first break and reflected wave tomographic inversion. From our point of view, this solves the trade-off between anisotropic and velocity parameters more effectively. We show a significant uplift in velocity model resolution after the incorporation of reflected wave energy into FWI. The resulting model resolution is comparable to that obtained in marine case studies.

Application of FWI to land data remains challenging due to the low signal-to-noise ratio, the presence of surface waves, near-surface heterogeneities, topography, and elastic effects. Over the past decade, Shell and Petroleum Development Oman (PDO) have investigated acquisition opportunities (Ten Kroode et al., 2013; Baeten et al., 2013a, 2013b; Plessix et al., 2012) leading to viable industrial solutions for broadband (> 1.5 Hz), long-offset and full-azimuth (FAZ) onshore acquisitions (Mahrooqi et al., 2012). Following these developments, several case studies have been published by Shell and PDO (Stopin et al., 2014, among others) showing great potential for FWI applications, particularly in Oman where standard migration velocity analysis is challenging due to a lack of strong reflections at depths shallower than one kilometre. In Stopin et al. (2014) it is proposed that the resulting FWI velocity model be used as a starting model for reflection-based tomography. Despite the undisputed success of the FWI case study, reliable model updates above 6 Hz were not obtained. The acoustic approximation was identified as the bottleneck (Solano et al., 2013), prompting investigations into the reliability of acoustic FWI (Plessix and Solano, 2015).

Here, rather than moving to elastic FWI, we investigate the impact of an improved acoustic FWI workflow to offset the prohibitive computational cost. We demonstrate that a high-resolution velocity model is obtainable with acoustic land FWI using reflected waves in addition to diving waves. Our land FWI workflow uses dedicated pre-processing of diving and refracted waves. We propose a two-stage approach (Figure 1),

[1] CGG
* Corresponding author, E-mail: anna.sedova@cgg.com

initially focusing on refractions and diving waves to reconstruct the long-wavelength components of the velocity model, and subsequently incorporating reflection energy to recover the medium-to-short spatial wavelength information, resulting in a model resolution comparable to marine FWI results.

We applied this workflow to a large broadband full-azimuth land data set acquired in the Sultanate of Oman by PDO. The data were acquired in 2014 using an acquisition design developed by PDO and Shell (Mahrooqi et al., 2012). The broadband 3D vibroseis survey used a nine-second sweep from 1.5 to 86 Hz, with full azimuths and large offsets.

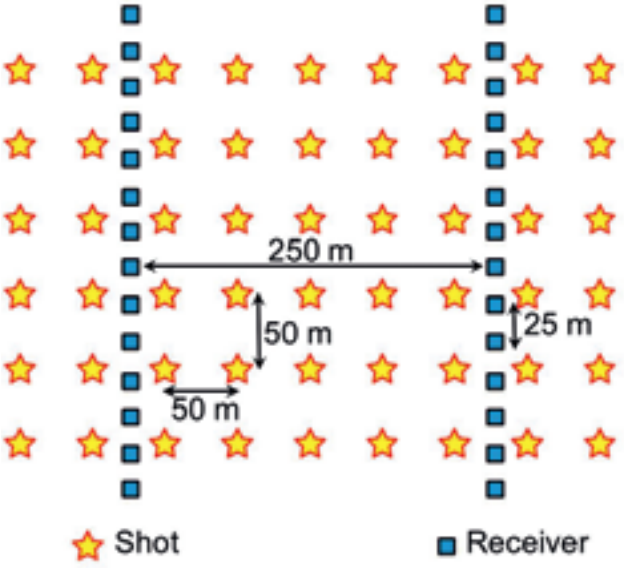

Figure 2 Close-up of the acquisition geometry of the survey. It is a full-azimuth, large-offset (up to 30 km acquired, though we only use up to 15 km in this study) and high-density acquisition. The source is vibroseis with a 9-second sweep of 1.5 to 86 Hz.

The dense acquisition design is very similar to that of Stopin et al. (2014) with a shot spacing of 50 m x 50 m, a receiver line interval of 250 m, a receiver spacing of 25 m (Figure 2) and distance-separated simultaneous sweeping (Bouska, 2010). The maximum offset recorded in the field is approximately 30 km but we limited it to 15 km for the processing of diving waves in order to ensure good signal-to-noise ratio for this application. The surface area imaged in this study spans 800 km^2.

Our FWI workflow retains some steps of reflection tomography, which provided velocity model updates in areas where conventional FWI fails, i.e. below or out of the limit of penetration of recorded diving waves. For the anisotropy estimation we do not rely on an anisotropic multi-parameter FWI as in Stopin et al. (2014). We believe that the anisotropy distribution should be obtained through a process that fits the kinematics of the diving and reflected waves jointly in order to better decouple the vertical and horizontal components of the velocity. We used a joint reflection and first-break tomographic inversion (Allemand et al., 2017) and then kept the anisotropic parameters fixed during the FWI update.

The FWI workflow presented here contains two main stages. We demonstrate in the first stage that the quality of the acoustic FWI velocity model, based on transmitted energy, can be improved by investing more effort into the refraction/diving wave pre-processing, up to 9 Hz. The second stage of the workflow (refraction and reflection FWI) incorporates more reflection data, which dramatically increases the subsurface resolution of the velocity model (up to 13 Hz).

High-frequency acoustic land FWI of diving waves

Our objective was to increase the resolution of the velocity model obtained by FWI while maintaining the acoustic approximation. This is possible if we incorporate reflection

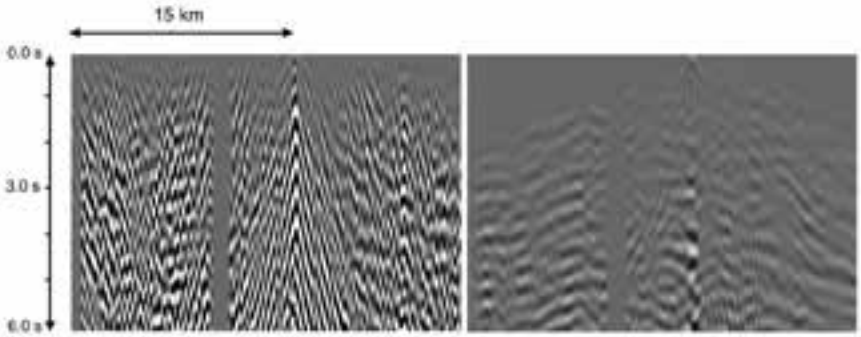

Figure 3 Removing ground roll. Application of surface wave attenuation to the first octave (0-2 Hz) of the land data; input (left) and output (right); the data are sorted in the cross-spread domain.

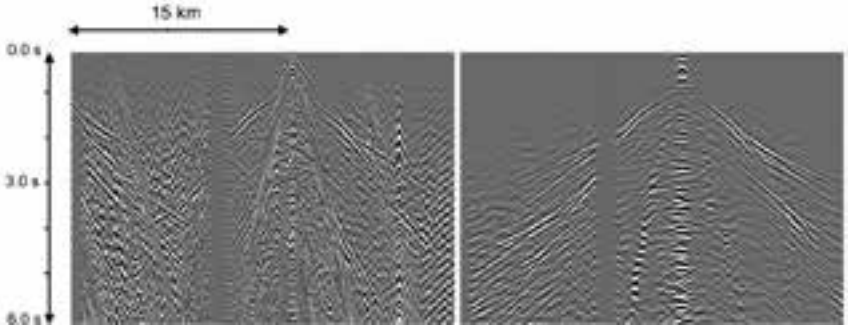

Figure 4 Mitigating simultaneous source cross-talk and near-surface noise. Application of joint low-rank sparse inversion to the second octave (2-4 Hz) of the land data; input (left) and output (right); the data are sorted in the cross-spread domain.

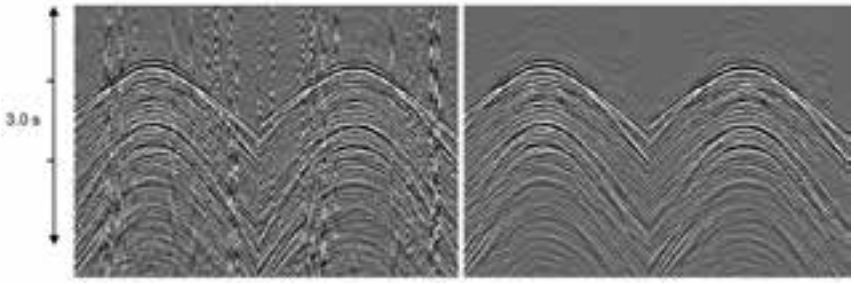

Figure 5 Enhancing lateral coherency. The final signal enhancement step was achieved by application of 3D linear noise filtering; full-bandwidth data input (left) and output (right); the data are sorted in the receiver domain.

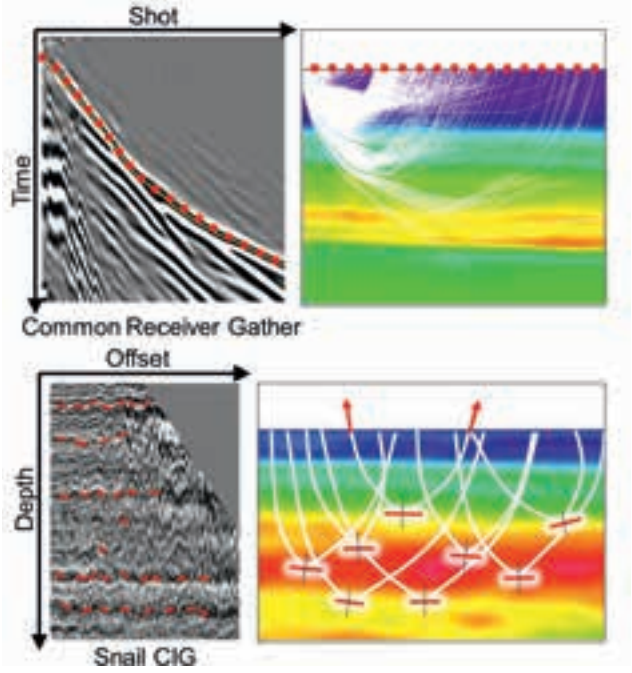

Figure 6 Joint reflection and diving wave tomography. Common receiver gather with first-break picking (top left) and corresponding diving ray paths (top right); Snail (pre-stack depth migrated traces sorted by increasing offset and azimuth) Common Image Gather (CIG) with residual moveout picks (bottom left) and corresponding reflected ray paths (bottom right) used jointly in reflection — diving wave tomography.

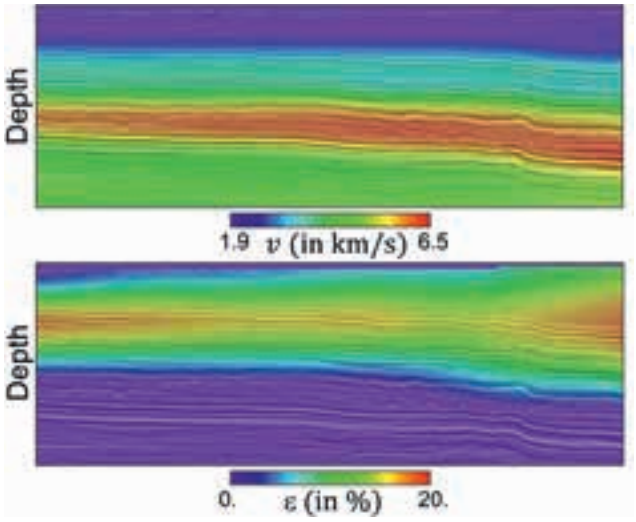

Figure 7 Joint tomography model. The velocity (top) and ε (right) models obtained by joint first-break and reflection tomographic inversion, with additional well information for δ.

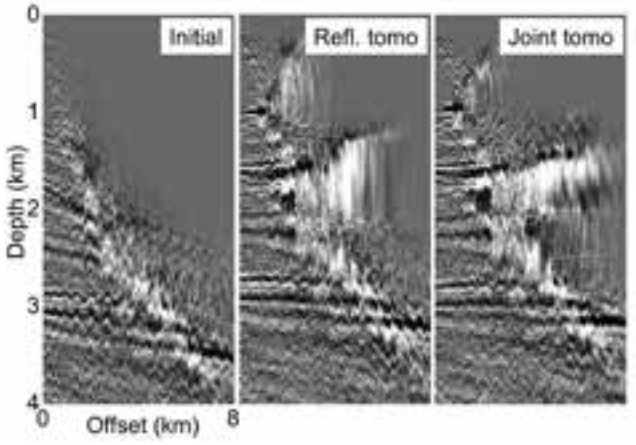

Figure 8 CIGs in the joint tomography model. For comparison purposes, we show a snail CIG: with the initial model (left); with the velocity model resulting from reflected wave tomography (centre); with a velocity model resulting from joint reflection – first-break tomography (right).

data and higher data frequencies into the inversion. Stopin et al. (2014) observed strong artifacts when incorporating data frequencies above 5.5 Hz, which were attributed to limitations of the acoustic assumption. We first investigated if more effective denoising could produce a reliable FWI result for diving waves at higher frequencies. The critical aspect of the broadband pre-processing sequences was the tuning of processing parameters at each frequency octave (Retailleau et al., 2014).

The raw data were strongly polluted by ground roll which could not be inverted by an acoustic FWI. In the first octave (0-2 Hz), ground roll energy dominates the signal. The application of adaptive surface wave attenuation (Le Meur et al., 2008) efficiently suppressed the ground roll at low frequencies (Figure 3).

Another challenge of the pre-processing sequence was the elimination of strong shot cross-talk (Figure 4 (left)), notably at long offsets, caused by simultaneous vibroseis sweeping (Bouska, 2010). This pre-processing step is not a part of the conventional reflection data pre-processing workflow which focuses on shorter offsets. To preserve our offset range we applied joint low-rank sparse inversion (Sternfels et al., 2015), which also eliminates noise resulting from human and industrial activity (Figure 4).

Finally, we used 3D linear noise filtering (Hugonnet et al., 2012) to eliminate residual noise (Figure 5).

At this point we were ready to apply diving wave FWI. Following Stopin et al. (2014), we applied an acoustic VTI formulation parameterized in pressure. The insertion of vector forces at source positions, and the conversion of pressure to particle

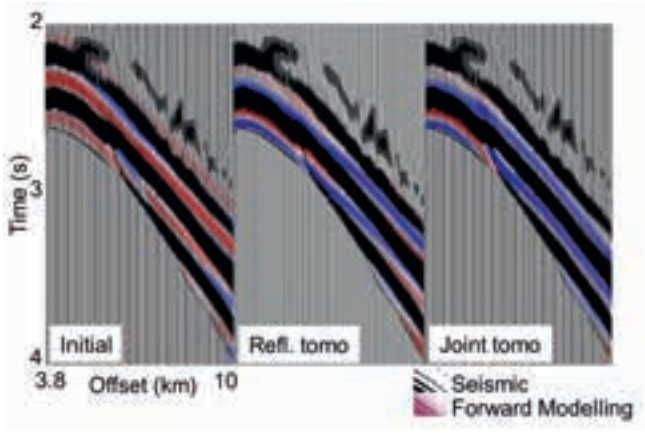

Figure 9 QC of diving waves after joint tomography. We superimpose the observed data (muted around diving waves) as black wiggle-traces with the synthetic wavefield obtained by acoustic wave propagation in blue/red using: the initial model (left); the velocity model resulting from reflected wave tomography (centre); the velocity model resulting from joint reflection – first-break tomography (right).

velocities at receiver positions, was managed by artificially submerging the source and receiver positions slightly below the free surface (Stopin et al., 2014; Sedova et al., 2017). Source-receiver reciprocity is implemented in order to optimize efficiency.

As FWI is driven mainly by the kinematics of diving waves, the resulting velocity models do not always flatten common image gathers. This is generally interpreted as the result of poorly estimated anisotropic parameters (Mothi et al., 2014). To estimate them, we used ray-based tomography to jointly invert for first breaks and the residual moveout representing the curvature of reflected events (Allemand et al., 2017). Joint tomography, taking into account a wide variety of ray paths (first breaks contain information from rays travelling mostly horizontally and reflected events from rays travelling nearly vertically), efficiently decouples the velocity and anisotropic parameters (Figure 6). The use of a non-linear algorithm for the joint inversion, based on non-linear slope tomography (Guillaume et al., 2008), is a key component ensuring the efficiency and accuracy of this approach.

Our model is parameterized in vertical velocity (V_v) and Thomsen's anisotropy parameters ε and δ. Figure 7 shows a section of the velocity and ε models obtained by joint reflection and first-break tomography (δ was obtained from well calibration). For comparison purposes, tomography was applied twice to update V_v and ε from the same initial models: initially using reflections only, and subsequently using reflections and first breaks jointly. CIGs are shown in Figure 8. Acoustic diving wave synthetics are shown in Figure 9, where the observed data (black wiggle) is superimposed over the wave-equation modelling (red-white-blue). A good kinematic fit is obtained when the red is hidden below the black wiggle making the blue predominant. Both reflection tomography and joint reflection and first-break tomography achieve flat gathers, but only the latter correctly recovers the diving wave kinematics. This gives us confidence in the method: flat CIGs and honoured first-break travel-times indicate that the estimated V_v and ε are reliable. We used the model obtained by joint tomography as an input for the first FWI step (the anisotropic parameters were kept fixed during FWI).

We applied tight inner and outer mutes to select refraction/diving waves for the first stage of the FWI workflow. The mutes applied at the second stage (refraction/reflection FWI) were much less selective (Figure 10). A maximum offset of 15 km was used for the first stage and 8 km for the second stage of FWI.

We incremented the maximum frequency from 3 to 9 Hz with 1 Hz steps and performed seven iterations at each frequency. The FWI convergence was good up to 9 Hz, as illustrated by the QCs

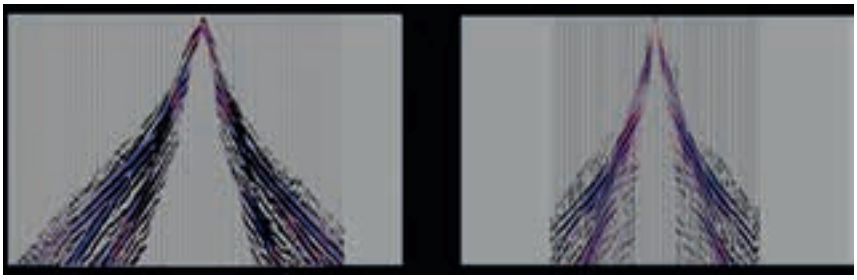

Figure 10 Data selection for FWI. Here we present the data selection and mute applied at different steps in the FWI workflow: refraction FWI at 9Hz (left); refraction/reflection FWI at 9 Hz (right).

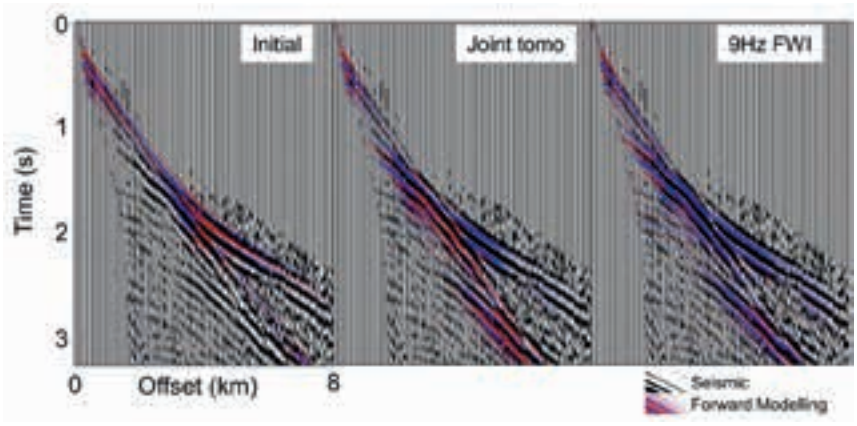

Figure 11 QC of diving waves after diving wave FWI at 9 Hz. We superimpose the observed data (muted around diving waves) as black wiggle-traces with the synthetic wavefield obtained by acoustic wave propagation in blue/red using: the initial model (left), the velocity model resulting from joint tomography (centre) and the velocity model resulting from FWI at 9 Hz (right).

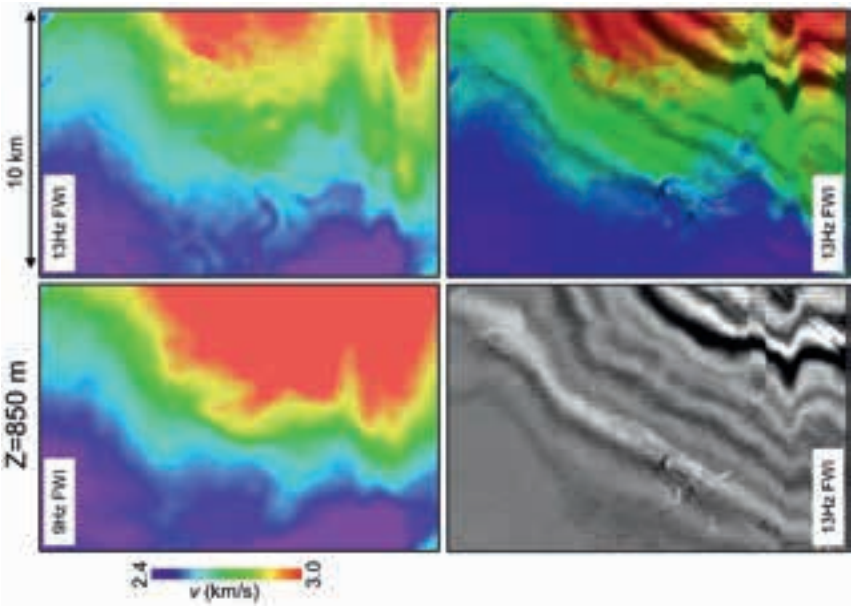

Figure 12 Common depth slice at Z=850 m. Top left: velocity model obtained by 9 Hz diving wave – refraction FWI. Top right: 13 Hz FWI result which incorporates reflections. The bottom images show the migrated stack using the 13 Hz FWI result, and the overlay highlights the degree to which it aligns with the velocity model.

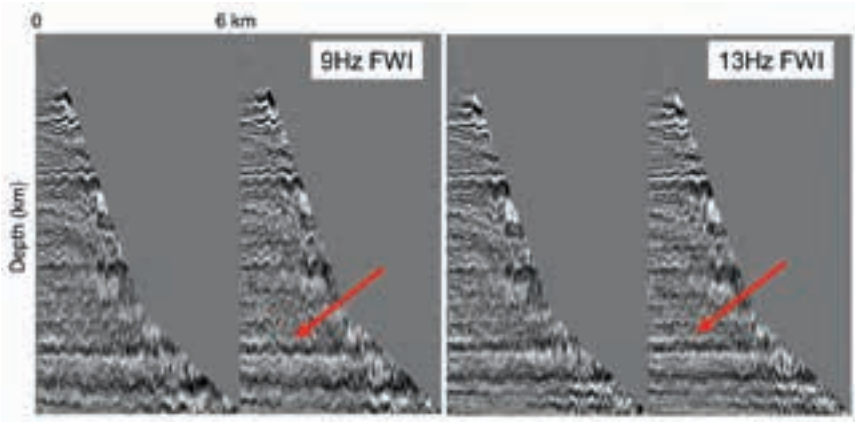

Figure 13 Snail CIGs before and after 13 Hz FWI. The snail CIGs migrated with the 9 Hz FWI velocity model obtained by inverting diving/refracted waves (left). The snail CIGs migrated with the 13 Hz FWI model obtained by inverting diving/refracted and reflected waves (right). We observe a significant increase in the flatness of the reflector, which we can interpret as a result of the high-resolution velocity structures added in the velocity model (see Figure 12).

comparing the real data and synthetics generated with the corresponding FWI model (Figure 11). Here again, a good kinematic fit is obtained when the black wiggle covers the red colour and the blue is predominant.

The resolution of the FWI result, even at 9 Hz, is limited because we used only refracted and diving waves (Figure 10, left). To increase the resolution we incorporated reflected energy, which is the second stage of the workflow.

High-frequency acoustic land FWI of diving and reflected waves

The second stage of our high-frequency land FWI workflow incorporated reflected waves. The input data were taken through a conventional depth migration data pre-processing workflow tailored for reflection energy. The maximum offset was reduced to 8 km (as in conventional pre-processing) and we adapted the mute applied (Figure 10) to preserve the diving and refracted wave content while adding reflected wave energy. The output FWI result from the first stage (9 Hz FWI) was used as the starting model for the second stage of FWI. The deeper part of the model not illuminated by recorded diving waves (shown in the top image of Figure 6) was updated by reflection tomography. FWI was applied to reflection/refraction data from 6 to 13 Hz, incremented by 1 Hz and with seven iterations at each frequency range.

Adding reflected data and increasing the data frequencies significantly improved both the resolution of the velocity model (Figure 12, top right) and the focusing of the migrated image. Figure 13 shows a comparison of snail CIGs before and after our second stage of FWI (9 Hz FWI versus 13 Hz FWI). We observed that the reflector (indicated by the red arrow) is significantly flatter and more coherent when these details are added in the velocity model.

We compared migrated stacks generated using the legacy velocity model obtained by conventional ray-based tomography through Migration Velocity Analysis (MVA) to migrated stacks generated using the 13 Hz FWI result. A stacked cross-line is shown in Figure 14. We observe an improvement in reflector continuity and focusing, particularly below the faulted structures (see red arrows on Figure 14) and in the deeper part of the section. In particular, the stack migrated with the 13 Hz FWI model resolved deeper faulting structures that are not apparent using the conventional velocity model building approach.

We observed a consistent alignment between details shown by the depth-migrated stack and the 13 Hz FWI velocity model. In Figures 15 and 16, we show depth slices of the final velocity

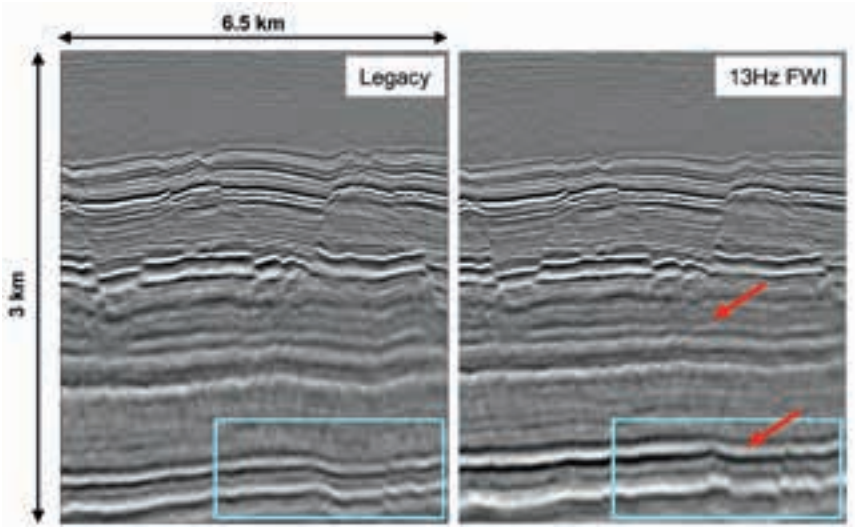

Figure 14 Comparison of legacy and 13 Hz FWI migration stacks. Cross-line of the migrated stack using: the legacy velocity model obtained by conventional MVA (left); the 13 Hz FWI velocity model (right).

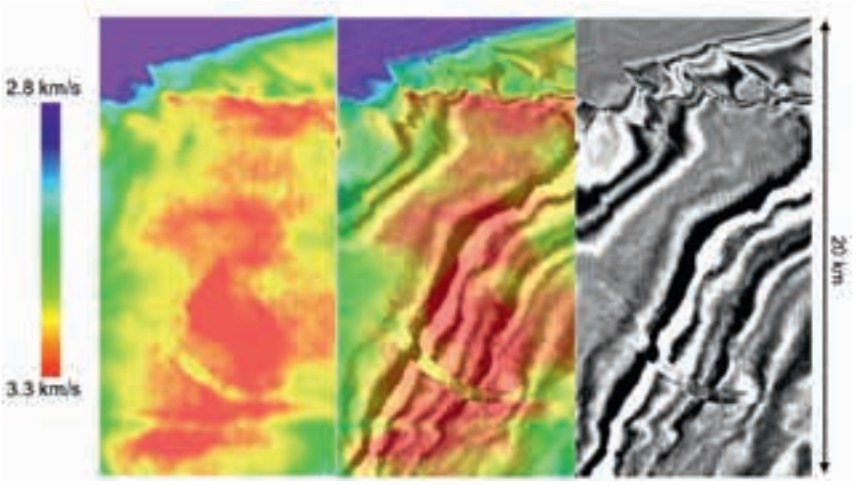

Figure 15 Common depth slice at Z=1000 m. From left to right: the final velocity (13 Hz FWI) model, the final velocity model overlaid on the depth-migrated stack, and the depth-migrated stack.

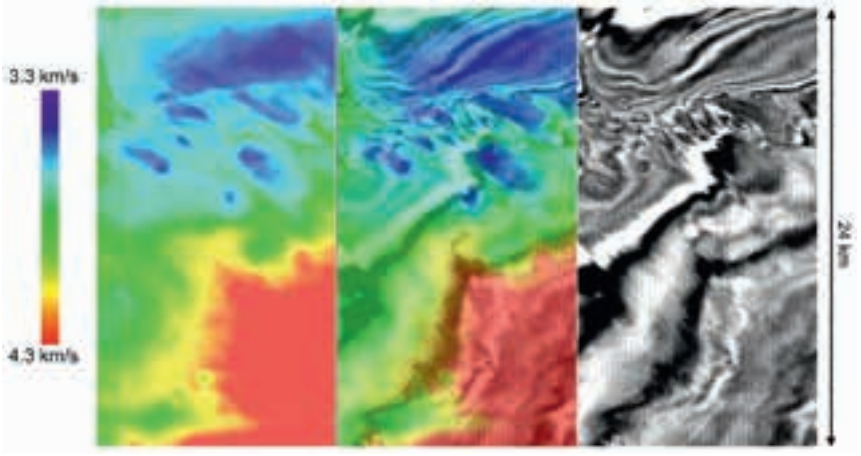

Figure 16 Common depth slice at Z=1500 m. From left to right: the final velocity (13 Hz FWI) model, the final velocity model overlaid on the depth-migrated stack, and the depth-migrated stack.

model and migrated stack at 1000 m and 1500 m, respectively. We see that our 13 Hz FWI result has recovered fine details such as buried channels and faults that align well with the migrated image.

Conclusions

We present an innovative acoustic land FWI workflow. Its application on a broadband FAZ land data set from the Sultanate of Oman illustrates the ability of acoustic FWI to deliver high-resolution, high-quality results that rival those typically seen from marine acquisitions. This success is attributed to improved data pre-processing, which aims to enhance the coherency of diving and refracted waves and remove ground roll, and to the introduction of carefully pre-processed reflection energy into FWI. The estimation of anisotropy by joint reflected and diving wave tomography to build the initial model was also essential as it jointly recovers the diving wave kinematics and flattens the CIGs.

This case study demonstrates that acoustic FWI, when combined with a workflow designed to enhance data quality, recover diving wave and reflection kinematics and flatten CIGs simultaneously, is a capable and computationally feasible tool for onshore full-azimuth surveys. The higher frequencies possible with acoustic FWI relative to elastic FWI lead to high-resolution and high-quality results, conventionally only seen in offshore acquisitions.

Acknowledgements

We are grateful to PDO and the Ministry of Oil and Gas of the Sultanate of Oman for providing data and permission to present these results. We would also like to thank Matthieu Retailleau, Botao Qin, David Le Meur, Milad Bader, Mathieu Reinier, Patrice Guillaume and Eric Suaudeau for many helpful insights and discussions, as well as CGG for permission to present this work.

References

Allemand, T., A. Sedova, A. and Hermant, O. [2017]. Flattening common image gathers after full-waveform inversion. The challenge of anisotropy estimation. *SEG Technical Program Expanded Abstracts*, 1410-1415.

Baeten, G., ten Kroode, F., Rawahi, S. and Mahrooqi, S. [2013a]. Onshore Low Frequency Acquisition for Full Waveform Inversion– from Field Trials to State of the Art Production Surveys. *75th EAGE Conference & Exhibition*, I07.

Baeten, G., de Maag, J.-W., Plessix, R.-E., Klaassen, R., Qureshi, T., Kleemeyer, M., ten Kroode, F. and Rujie, Z. [2013b]. The use of low frequencies in a full-waveform inversion and impedance inversion land seismic case study. *Geophysical Prospecting*, **61**, 701–711 doi: 10.1111/1365-2478.12010.

Bouska, J. [2010]. Distance separated simultaneous sweeping, for fast, clean, vibroseis acquisition. *Geophysical Prospecting*, **58**, 123–153.

Guillaume, P., Lambaré, G., Leblanc, O., Mitouard, P., Le Moigne, J., Montel, J.-P., Prescott, T., Siliqi, R., Vidal, N., Zhang, X. and Zimine, S. [2008]. Kinematic invariants. An efficient and flexible approach for velocity model building. *78th Annual International Meeting, SEG*, Expanded Abstracts, 3678–3692.

Hugonnet, P., Boelle J.L. and Prat F., [2012]. Local linear events extraction and filtering in the presence of time-shifts. *74th EAGE Conference & Exhibition*, Expanded Abstracts, I024.

Le Meur, D., Benjamin, N., Cole, R. and Al Harthy, M. [2008]. Adaptive groundroll filtering. *70th EAGE Conference & Exhibition*, Expanded Abstracts, G036.

Mahrooqi, S., Rawahi, S., Yarubi, S., Abri, S., Yahyai, A., Jahdhami, M., Hunt, K. and Shorter, J. [2012]. Land seismic low frequencies. Acquisition, processing and full wave inversion of 1.5-86 Hz. *82nd Annual International Meeting, SEG*, Expanded Abstracts, 1-5.

Mei, J., Ahmed, S., Searle, A. and Ting, C-O., [2014]. FWI Application on an Alaska Land 3D Survey. *SEG Technical Program*, Expanded Abstracts, 981-986.

Mothi, S., Bi, H., and Yang, A. [2012]. Benefits of FWI in Prestack Depth Imaging of Onshore Data. a Gulf Coast example. *SEG Technical Program,* Expanded Abstracts, 4205-4210

Mothi, S. and Kumar, R. [2014]. Detecting and estimating anisotropy errors using full waveform inversion and ray-based tomography. A case study using long-offset acquisition in the Gulf of Mexico. *84th Annual International Meeting, SEG*, Expanded Abstract, 1066-1071.

Plessix, R.-E., Baeten, G., de Maag, J.W., ten Kroode, F. and Rujie, Z. [2012]. Full waveform inversion and distance separated simultaneous sweeping. a study with a land seismic data set. *Geophysical Prospecting*, **60** (4), 733–747, doi: 10.1111/j.1365-2478.2011.01036.x.

Plessix, R.É. and Solano, C.A.P. [2015]. Modified surface boundary conditions for elastic waveform inversion of low-frequency wide-angle active land seismic data. *Geophysical Journal International*, **201**(3), 1324–1334.

Retailleau, M., El Asrag, R. and Shorter, J. [2014]. Processing land broadband data. results and challenges on Oman surveys. *SPG/EAGE workshop on Broadband Seismic,* Extended Abstracts.

Sedova, A., Royle, G., Hermant, O., Retailleau, M. and Lambaré, G. [2017]. High-resolution land full-waveform inversion. a case study on a data set from the Sultanate of Oman. *79th Conference and Exhibition, EAGE*, Extended Abstracts, We A3 04.

Solano, C. A. P., Stopin, A. and Plessix, R.-E. [2013]. Synthetic study of elastic effects on acoustic full waveform inversion. *75th International Conference and Exhibition*, EAGE, Extended Abstracts, P10.

Sternfels, R., Viguier, G., Gondoin R. and Le Meur, D. [2015]. Multidimensional simultaneous random plus erratic noise attenuation and interpolation for seismic data by joint low-rank and sparse inversion. *Geophysics*, **80** (6), WD129-WD141.

Stopin, A., Plessix, R.-E. and Said, A.A. [2014]. Multiparameter waveform inversion of a large wide azimuth low-frequency land data set in Oman. *Geophysics*, **79**(3), WA67-WA77.

Ten Kroode, A. P. E., Bergler, S., Corsten, C., de Maag, J. W., Strijbos, F. and Tijhof, H. [2013]. Broadband seismic data. The importance of low frequencies. *Geophysics*, **78** (2), WA3–WA14, doi: 10.1190/geo2012-0294.1.